

Article

# Combining a New Parameterization Scheme of Oceanic Heat Flux with Thickness Assimilation to Improve Sea Ice Forecast Accuracy in Liaodong Bay

Binhang Wei <sup>1</sup>, Baohui Li <sup>1</sup>, Jiechen Zhao <sup>2,3</sup>, Yu Liu <sup>1</sup>, Zhijun Wei <sup>4</sup> and Anliang Wang <sup>1,\*</sup> 

<sup>1</sup> Key Laboratory of Marine Hazards Forecasting Ministry of Natural Resources, National Marine Environmental Forecasting Center, Beijing 100081, China; wbh12419957@163.com (B.W.); libh@nmefc.cn (B.L.); liuyu@nmefc.cn (Y.L.)

<sup>2</sup> Qingdao Innovation and Development Base of Harbin Engineering University, Qingdao 266400, China; zhaojiechen@hrbeu.edu.cn

<sup>3</sup> Key Laboratory for Polar Acoustics and Application of Ministry of Education, Harbin Engineering University, Harbin 150001, China

<sup>4</sup> State Key Laboratory of Coastal and Offshore Engineering, Dalian University of Technology, Dalian 116024, China; wzjdlut@dlut.edu.cn

\* Correspondence: wangal@nmefc.cn; Tel.: +86-010-6210-5750

**Abstract:** Liaodong Bay is one of the lowest latitude areas with seasonal sea ice cover in the Northern Hemisphere. Sea ice forecasting faces challenges in accuracy due to its low thickness. Therefore, a novel parameterization scheme for oceanic heat flux was developed to forecast sea ice thickness accurately. Application of the parameterization scheme for oceanic heat flux in the HIGHTSI model significantly improved the forecasting accuracy of sea ice thickness before the severe ice period. During this period, the RMSE of sea ice thickness measured on the JZ9–3 and the JZ20–2 oil platforms decreased by 0.53 cm and 2.90 cm compared to previous schemes, respectively. In order to improve the forecasting accuracy during the severe and melting ice periods, the observed and retrieved sea ice thickness was nudged into the model. The simulated results demonstrated a good agreement with monitored sea ice thickness distribution. During the entire season with sea ice cover, the R-squared values between simulated and retrieved sea ice thickness in the core area of Liaodong Bay reached 0.76. Furthermore, this study revealed a relatively strong correlation between air temperature and ice temperature on the following day. The proposed scheme provides a valuable approach to improve the forecasting accuracy for the areas with low thickness in the sea ice numerical models.

**Keywords:** sea ice; Liaodong Bay; oceanic heat flux; parameterization; nudging



**Citation:** Wei, B.; Li, B.; Zhao, J.; Liu, Y.; Wei, Z.; Wang, A. Combining a New Parameterization Scheme of Oceanic Heat Flux with Thickness Assimilation to Improve Sea Ice Forecast Accuracy in Liaodong Bay. *J. Mar. Sci. Eng.* **2023**, *11*, 2306. <https://doi.org/10.3390/jmse11122306>

Academic Editor: Anatoly Gusev

Received: 4 October 2023

Revised: 14 November 2023

Accepted: 16 November 2023

Published: 6 December 2023



**Copyright:** © 2023 by the authors. Licensee MDPI, Basel, Switzerland. This article is an open access article distributed under the terms and conditions of the Creative Commons Attribution (CC BY) license (<https://creativecommons.org/licenses/by/4.0/>).

## 1. Introduction

Liaodong Bay is the most severe area with sea ice cover in the Bohai Sea during the winter season. Nevertheless, the sea ice thickness in this area remains relatively thin, typically ranging from 10 to 20 cm during severe ice periods [1]. During the initial and melting ice periods, the sea ice thickness decreases to just a few centimeters. On a small spatial and temporal scale, sea ice thermodynamics are notably influenced by local weather and ocean conditions, such as cold wind, storm waves, and sea surface temperature [2,3]. Hence, the sea ice forecast in Liaodong Bay poses a challenge for the sea ice numerical model. Additionally, global warming, accompanied by extreme weather conditions, makes the forecast of sea ice growth and melting more difficult [4,5]. The duration and concentration of sea ice in seasonal ice zones at mid-latitudes have been decreasing over the past few decades [6]. Thermodynamic processes play a crucial role in the variability of the mid-latitude cryosphere [7,8]. The influence of climate change could be reflected effectively by the growth and melting of sea ice [9]. Consequently, sea ice thermodynamic processes play

a crucial role in the numerical prediction of sea ice and provide the physical foundation for sea ice thermodynamic models.

Maykut and Untersteiner (1971) pioneered the sea ice thermodynamic model [10]. The internal heating of the ice layer and solar transmittance radiation were considered in this model. However, the latent heat calculation on the upper and lower surfaces of the sea ice was found to violate the law of energy conservation. This model played an indispensable role in the advancement of sea ice thermodynamic models. For forecasting sea ice accurately in small-scaled regions, the HIGHTSI (high-resolution thermodynamic snow and ice) model was proposed by Launiainen and Cheng [11]. The HIGHTSI model incorporates a shorter time step for more precise calculations. Additionally, it features a variable vertical resolution of ice layers to enhance its accuracy in high-resolution simulations. It considers various processes, including surface heat balance, internal heat conservation in ice and snow, and heat conduction at the ice bottom. The model has been successfully applied for sea ice forecast purposes in the Baltic Sea, Kara Sea, Polynya, Zhongshan Station, and Prydz Bay [12–18]. This application shows a promising future for the HIGHTSI model in the sea ice forecast of local regions.

Sea ice thermodynamic processes encompass internal heat conduction within the ice, thermal equilibrium at the ice–air interface, and heat exchange at the ice–ocean boundary. The heat transferred from the seawater to the ice bottom during turbulent heat exchange is known as the oceanic heat flux. The oceanic heat flux is a pivotal component in the energy and mass balance of sea ice. In large-scale and multi-year ice regions, the oceanic heat flux was typically assumed to be a constant [19]. However, high-latitude regions dominated by first-year ice, such as the Okhotsk Sea, East Greenland Sea, and Amundsen Sea, exhibit significant spatiotemporal variations in the oceanic heat flux throughout different seasons [20–25]. Liaodong Bay is one of the lowest latitude areas with seasonal sea ice cover in the Northern Hemisphere. The area of Liaodong Bay accounts for about 2% of the area of the Arctic Ocean and about 40% of the total area of the Bohai Sea. It experiences significant sea surface heat exchange and vertical convective mixing due to its distinctive geographical location and relatively limited spatial scale. Hence, oceanic heat flux with high temporal resolution can simulate the growth and melting of sea ice in detail. Ma et al. [26] categorized the oceanic heat flux into distinct values, considering the initial ice period, severe ice period, and melting ice period. Other researchers proposed oceanic heat flux with temporal resolutions of 3 days and 1 day for Liaodong Bay [27,28]. The most detailed characterization of oceanic heat flux had a temporal resolution of 2 h [29]. The determination of appropriate timescales for oceanic heat flux in small-scale regions was intricately linked to the numerical simulations in studying sea ice thermodynamics.

One of the ways to improve the quality of sea ice forecast is data assimilation, as small-scale regions accompanied by thinner sea ice pose challenges in sea ice prediction. Different techniques, including ghost-flux forcing [30–32], ice-coupling forcing [33,34], and direct nudging [35], are employed to constrain simulation errors within a narrower range. Ghost-flux forcing and ice-coupling forcing assimilate sea ice thickness and sea ice concentration into the oceanic heat flux by nudging techniques [36]. Both of them incorporate sea ice concentration data. In contrast, the HIGHTSI model does not encompass the characterization of sea ice concentration. Furthermore, the calculation of nudging oceanic heat flux involves a plethora of parameters. Unstable fluctuations of the oceanic heat flux may lead to significant errors in the simulation. Direct sea ice nudging is a technique that involves the introduction of an initial ice thickness value, facilitating sea ice thickness forecasting precisely and timely.

In this study, we implemented a parameterized scheme for the oceanic heat flux in Liaodong Bay. The HIGHTSI model was conducted to simulate the sea ice thickness for the winter of 2021–2022. Moreover, the sea ice thickness prediction incorporated a nudging method. Our advancements in sea ice forecasting within the local region were evaluated by comparing the results with other parameterized methods. At the point level, the simulation was validated by the sea ice thickness observed on two oil platforms (JZ9–3 and JZ20–2) in

Liaodong Bay. The retrieved sea ice thickness from satellite images captured by MODIS and HY-1C/1D was also nudged into the simulation for better results both along a line and for the region. Finally, we examined the correlation between ice temperature and air temperature in Liaodong Bay.

## 2. Study Area and Data Source

### 2.1. Study Area

Liaodong Bay is situated within the latitude range of  $38^{\circ}44' \sim 40^{\circ}57' \text{ N}$  and longitude range of  $119^{\circ}16' \sim 122^{\circ}17' \text{ E}$ , with an approximate area of  $30,605 \text{ km}^2$ , as shown in Figure 1. Liaodong Bay is one of the three prominent bays in the Bohai Sea. It experiences the severest ice conditions during winter compared to other bays in the area. A typical season with sea ice cover in Liaodong Bay lasts from late November or early December to early March or mid-March. Over the past 20 years, the average annual maximum sea ice area in Liaodong Bay has been approximately  $14,948 \text{ km}^2$ . In recent years, the sea ice thickness in Liaodong Bay has ranged from 10 to 20 cm, with the maximum thickness along the coast not exceeding 35 cm.

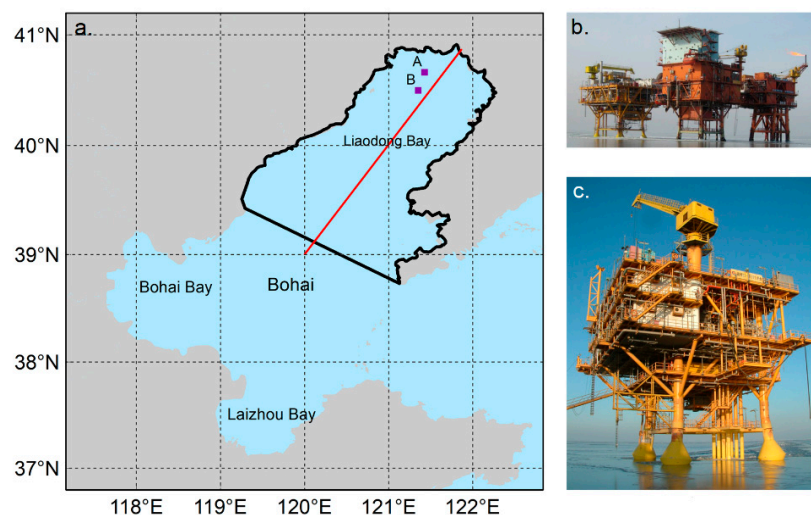


**Figure 1.** Location of the study area: (a) study area; (b) JZ20–2 oil platform; (c) JZ9–3 oil platform.

A baseline from  $40^{\circ}51' \text{ N}$ ,  $121^{\circ}52' \text{ E}$  to  $39^{\circ}00' \text{ N}$ ,  $120^{\circ}00' \text{ E}$  depicts the bay's sea ice distribution [37]. The extent of sea ice in the bay can be expressed as a distance along the baseline (red line in Figure 1) that crosses the area. Two oil platforms, JZ9–3 ( $40^{\circ}40' \text{ N}$ ,  $121^{\circ}28' \text{ E}$ ) and JZ20–2 ( $40^{\circ}30' \text{ N}$ ,  $121^{\circ}21' \text{ E}$ ), were used to monitor the sea ice conditions during the season with sea ice cover, as depicted by points A and B in Figure 1a. The data was analyzed for a study period from 1 December 2021 to 15 March 2022.

### 2.2. Data Source

#### 2.2.1. Meteorological Data

Meteorological data were obtained from the European Centre for Medium-Range Weather Forecasts (ECMWF) ERA5 hourly data on single levels from 1940 to the present [38]. 2-m temperature, 2-m dewpoint temperature, 10-m wind velocity, downwards surface thermal radiation, downwards surface solar radiation, and total cloud cover were selected as meteorological forcing fields during the winter in 2021–2022. These data are derived at a spatial resolution of  $1/4^{\circ}$  and a temporal resolution of 1 h.

#### 2.2.2. Seawater Data

The mixed layer temperature data were sourced from the Mercator Global Ocean Analysis and Forecasting System data [39]. The data have a spatial resolution of  $1/12^{\circ}$  and a temporal resolution of 6 h. We accessed the mixed layer temperature data from the Mercator

Global Ocean Analysis and Forecasting System (MGOAFS) data covering the winters of 1997–1998 and 2021–2022. Additionally, the National Marine Environmental Forecasting Center (NMEFC) provided ocean current velocity data with a temporal resolution of 1 h and a spatial resolution of  $1/20^\circ$  [40].

We interpolated the time series of 2-m temperature and mixed layer temperature of the two oil platforms during the winter of 2021–2022 in Figure 2. The 2-m temperature and mixed layer temperature of the two oil platforms were obtained through linear interpolation of data from neighboring grid points. Additionally, the mixed layer temperature was obtained at a temporal resolution of 1 h using linear interpolation techniques. The 2-m temperatures on both oil platforms were very similar due to the low spatial resolution of ERA5 data. The mixed layer temperature on the JZ9–3 oil platform was lower compared to that on the JZ20–2 oil platform before freezing. However, during the melting ice period, the mixed layer temperature became higher than that on the JZ20–2 oil platform.

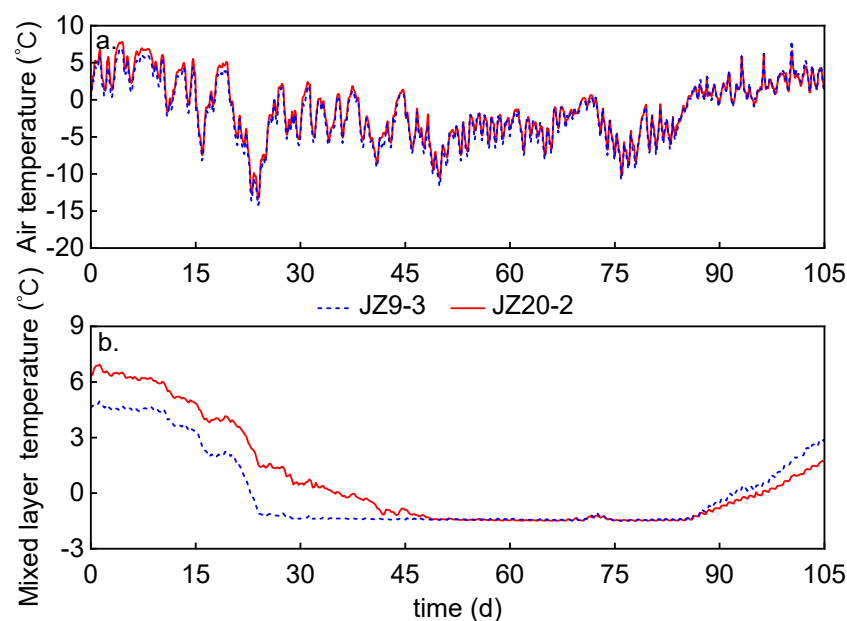


**Figure 2.** Time series of the air and mixed layer temperature on two oil platforms during the winter of 2021–2022. ((a) air temperature on two oil platforms; (b) mixed layer temperature on two oil platforms).

### 2.2.3. Sea Ice Data

The sea ice thickness observations on two oil platforms were collected on-site with a temporal resolution of 1 day, ranging from the 25th day (25 December 2021) to the 87th day (25 February 2022). The sea ice drift speed and retrieved sea ice thickness data were run at the NMEFC [40]. Sea ice drift speed data has a spatial resolution of  $1/30^\circ$  and a temporal resolution of 1 h. Retrieved sea ice thickness data, with a spatial resolution of  $1/10^\circ$  and a temporal resolution of 1 day, served as the initial values. All data were interpolated to a spatial resolution of  $1/12^\circ$  and a temporal resolution of 1 h by linear interpolation to ensure consistency. The maximum sea ice extent in Liaodong Bay occurred on the 79th day (17 February 2022) during the winter of 2021–2022. Figure 3 illustrates the 2-m air temperature, 10-m wind velocity, mixed layer temperature, and ocean current velocity in Liaodong Bay at 0:00 a.m. on the 79th day (17 February 2022).

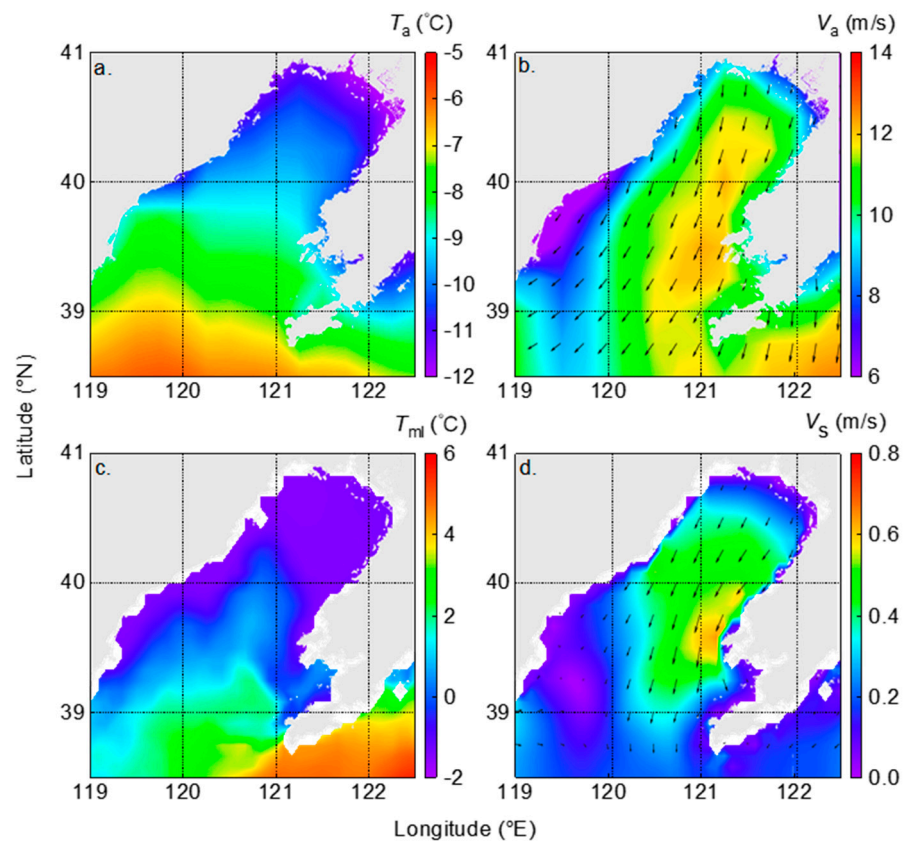


**Figure 3.** (a) 2-m air temperature, (b) 10-m wind velocity, (c) mixed layer temperature, and (d) ocean current velocity in Liaodong Bay at 0:00 a.m. on the 79th day (17 February 2022).

#### 2.2.4. Data Uncertainties

Although ERA5 exhibits good temporal resolution, its spatial resolution ( $0.25^\circ$ ) is coarse, considering the spatial scale of Liaodong Bay. Grid points near the coastline are particularly vulnerable to the influence of inland meteorological factors. Furthermore, sea-water data, especially the mixed layer temperature, sometimes cannot guarantee temporal continuity at an hourly level.

Sea ice thickness retrieval poses challenges due to the relatively low thickness in Liaodong Bay. Currently, some parameters used in retrieved algorithms are based on empirical values. Fluctuations in various parameters within these algorithms can result in discrepancies between retrieved and true values. For example, the Root Mean Squared Error (RMSE) between the observed and retrieved sea ice thickness was 3.80 cm and 4.27 cm on the JZ9–3 and the JZ20–2 oil platforms during the winter of 2021–2022, respectively. In this study, both the retrieval and on-site observation times were assumed to be uniform at 12:00 p.m. each day, introducing uncertainty to the nudging process.

### 3. Methods

At first, we proposed a parameterization scheme for oceanic heat flux applicable to Liaodong Bay based on Newton’s cooling law and the bulk formula. Then, the sea ice thickness was assimilated, and sea ice thickness was retrieved via nudging every 5 days. To evaluate our method, we conducted a comparison of our results to other studies and also validated the results against the remaining in situ observations not used for nudging.

#### 3.1. Sea Ice Model

The HIGHTSI model was applied to simulate sea ice thickness in Liaodong Bay. It aims to address the surface temperature of ice, internal temperature of ice, and sea ice thickness. The HIGHTSI model includes heat conduction within the ice, surface heat balance, and

heat balance at the ice bottom. Figure 4 shows the physical processes described in the HIGHTSI model. Solar radiation penetrates through the cloud layer and reaches the surface. The incoming short-wave radiation splits into two parts at the surface. A portion continues to penetrate into the ice layer, while the remaining fraction is reflected back into the atmosphere. Water vapor in the air absorbs long-wave radiation emitted from the surface and contributes to the downwelling atmospheric long-wave radiation. The sensible heat flux is controlled by the temperature difference between the ice and the surrounding air. Water vapor evaporation and sea ice melting are controlled by the latent heat flux. Temperature in ice layers is controlled by heat conduction. Ice bottom freezing and melting are controlled by the conductive heat flux and the oceanic heat flux at the ice–ocean interface.

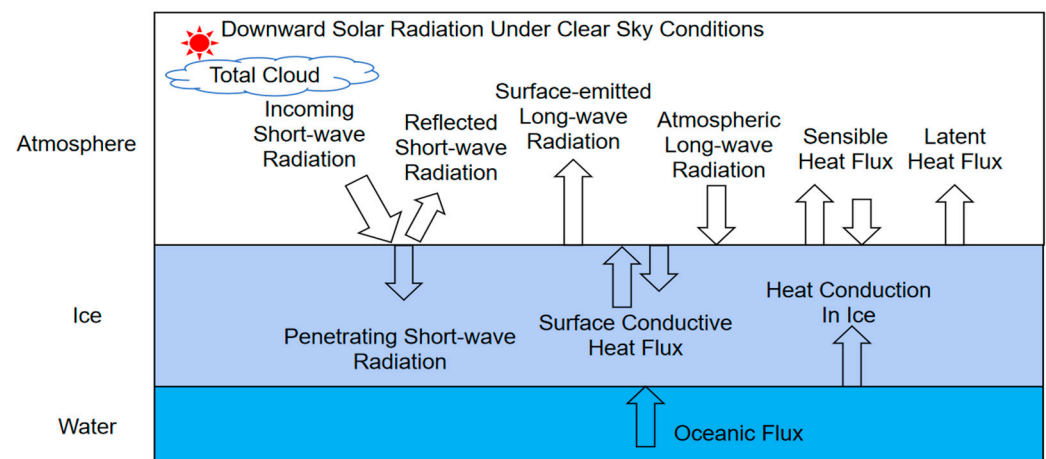


**Figure 4.** Physical processes described in the HIGHTSI model.

The downward direction represents the positive direction of radiation transmission. Incoming short-wave radiation only occurs during the daytime, with values ranging from 0 to several hundred  $\text{Wm}^{-2}$ . Surface-emitted long-wave radiation reaches approximately  $-280 \text{ Wm}^{-2}$  during the season with sea ice cover. Atmospheric long-wave radiation is slightly smaller than the absolute value of surface long-wave radiation. The values of the ice surface sensible heat flux range approximately from 50 to  $-400 \text{ Wm}^{-2}$ . Latent heat flux on the ice surface is smaller than sensible heat flux, around  $-50 \text{ Wm}^{-2}$ . Surface conductive heat flux and heat conduction in ice range from  $-100$  to  $-300 \text{ Wm}^{-2}$ . We will discuss the oceanic heat flux in detail in the following part.

Radiation fluxes are subject to the influence of various atmospheric properties, leading to a multifaceted relationship with the atmospheric column [12]. Simplified parameterization of radiation fluxes in models is computationally demanding [41]. We applied schemes proposed by Shine [42] to parameterize the downwelling short-wave radiation fluxes. The scheme proposed by Prata [43] was chosen to parameterize downwelling long-wave radiation fluxes. Cloud effects were accounted for using Bennett's [44] and Jacobs' [45] parameterization schemes. Bennett [44] provided an explanation for the impact of clouds on short-wave radiation, whereas Jacobs [45] addressed the influence of clouds on long-wave radiation. In this study, we assumed a constant freezing temperature ( $-1.8 \text{ }^\circ\text{C}$ ) and divided the sea ice into five layers. Solar radiation analysis incorporated cloud influence based on Grenfell and Maykut's [46] and Perovich's [47] schemes. The initial value of the sea ice thickness was assumed to be 0.001 m at the first time step to make the computation stable. The selection of most HIGHTSI model parameters was based on the work of Cheng [13]. The model parameters are presented in Table 1.

**Table 1.** Major parameters adopted by this paper.

Parameter	Meaning	Value
$c_w$ [23]	Coefficient of friction	0.0055
$T_f$	Freezing temperature	$-1.8\text{ }^\circ\text{C}$
$c_i$	Specific heat of ice	$2093\text{ J/kg}\cdot\text{K}$
$c_a$	Specific heat of air	$1004\text{ J/kg}\cdot\text{K}$
$L_f$	Latent heat of fusion	$3.36 \times 10^5\text{ J/kg}$
$\gamma_i$ [47]	Extinction coefficient of sea ice	$1.5\text{ m}^{-1}$
$k_i$	Heat conductivity of ice	$2.03\text{ W/m}\cdot\text{K}$
$S_s$	Seawater salinity	30
$\epsilon_i$	Surface emissivity	0.97
$\sigma_a$	Stefan–Boltzmann constant	$5.68\text{ W/m}^{-2}\cdot\text{K}$
$S$	Solar constant	$1367\text{ W/m}^{-2}$
$k_0$	Von–Karman constant	0.4
$N_{ice}$	Number of layers in the ice	5
$dt$	The time step of the simulation	1/24 day

### 3.2. Parameterization for Oceanic Heat Flux

The oceanic heat flux ( $F_w$ ) is interpreted as the measure of turbulent heat exchange occurring at the ice bottom. It plays a crucial role in the simulation of sea ice. In this study, the bulk formula was employed to estimate the oceanic heat flux [48,49]. The oceanic heat flux can be derived from Newton’s law of cooling  $Q = hA\Delta T$ . Where  $Q$  is convection heat transfer,  $h$  is the heat transfer coefficient,  $A$  denotes the area of the interface, and  $\Delta T$  is the disparity between two objects. Since the HIGHTSI model is a one-dimensional model,  $A$  is expressed as per unit area. The origin form of the bulk formula is

$$F_w = h\Delta T_m, \tag{1}$$

where  $\Delta T_m$  denotes the disparity between the mixed layer temperature and freezing temperature ( $-1.8\text{ }^\circ\text{C}$ ).  $h$  denotes the heat transfer coefficient [49].

$$h = \rho_w c_p c_h U_0^*, \tag{2}$$

where  $\rho_w = 1025\text{ kg/m}^3$  denotes the density of seawater,  $c_p$  denotes the specific heat of water. The friction velocity at the interface is derived from the Stokes’ law for quadratic drag,

$$U_0^{*2} = c_w U^2, \tag{3}$$

where  $c_w$  denotes a coefficient of friction, and  $U$  denotes the relative velocity between sea ice drift speed and ocean current speed. A value of 0.0055 was assumed for the coefficient [23].  $c_h$  denotes the heat exchange coefficient, different from the heat transfer coefficient ( $h$ ). However, the heat transfer coefficient is challenging to determine experimentally [50]. In most cases, inverse calculations are necessary to obtain the heat transfer coefficient [51]. Chen et al. [51] observed that the heat transfer coefficient ( $h$ ) demonstrated an exponential correlation with  $\Delta T_m$ . In Equation (2),  $\rho_w$ ,  $c_p$ ,  $U_0^*$  remains relatively stable with minor variations in  $\Delta T_m$ . Therefore, the heat exchange coefficients ( $c_h$ ) is correlated with  $\Delta T_m$ .

The determination of the heat exchange coefficient is crucial in heat transfer analysis, despite some scholars considering the heat exchange coefficient to be constant [52,53]. This coefficient has a direct impact on the calculation of oceanic heat flux and simulation. We were able to determine the heat exchange coefficient for the winter of 1997–1998 on the JZ20–2 oil platform [54] solely. In this study, we established a relationship between the heat exchange coefficient ( $c_h$ ) and the disparity between the mixed layer temperature [39] and the freezing temperature, as shown in Figure 5. The heat exchange coefficient ( $c_h$ ) was measured on the JZ20–2 oil platform during the winter of 1997–1998 [54]. The disparity between the mixed layer temperatures was obtained through the MGOAFS dataset [39].

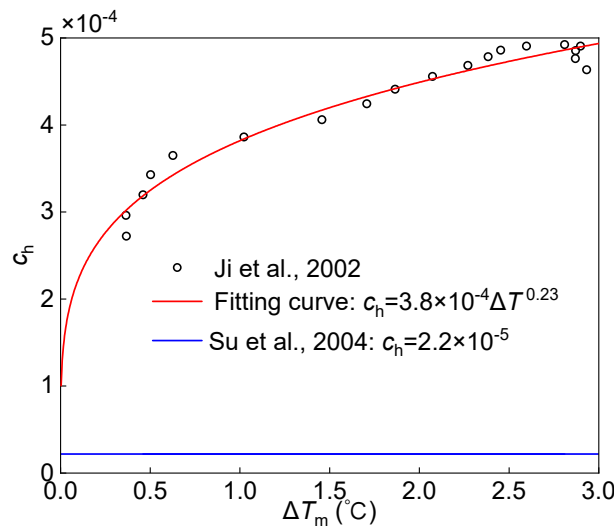


Figure 5. Relationship between the mixed layer temperature and the heat exchange coefficient. [52,54].

A larger value of  $\Delta T_m$  indicates a robust heat exchange process between the sea ice and seawater. Correspondingly, the magnitude of the heat exchange coefficient is relatively high in this particular scenario. Conversely, the heat exchange coefficient experienced a rapid decline as the equilibrium between sea ice and seawater was approached. Finally, we derived a parameterized formula for the oceanic heat flux.

$$F_w = 2.1 \times 10^{-6} \rho_s c_p U^2 \Delta T_m^{1.23}, \tag{4}$$

Then, the oceanic heat flux scheme was used on the JZ9-3 (Figure 6a) and JZ20-2 (Figure 6b) platforms during the winter of 2021–2022. Notably, oceanic heat flux had significant differences in different ice periods. The JZ20-2 platform started to freeze on the 40th day (9 January 2022) through observation. The intense heat exchange between seawater and sea ice in the initial ice period leads to large values of the oceanic heat flux. The JZ9-3 platform became frozen on the 25th day (25 December 2021) through observation, earlier than that of the JZ20-2 platform. Oceanic heat flux did not exceed  $10 \text{ Wm}^{-2}$  during the severe ice period in our parameterization scheme. However, the oceanic heat flux increased to  $10\text{--}20 \text{ Wm}^{-2}$  during ice melting due to the increase of  $\Delta T_m$ . This process was slow and could be attributed to the presence of an ice layer separating the seawater and the atmosphere.

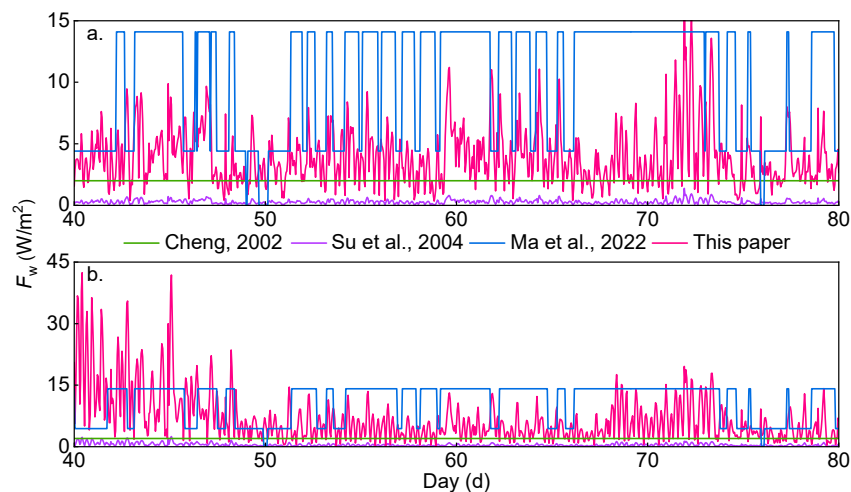


Figure 6. The oceanic heat flux adopted by different parameterization schemes on (a) the JZ9-3 and (b) the JZ20-2 platforms [13,26,52].

Meanwhile, Figure 6 also shows the parameterized oceanic heat flux using other schemes [13,26,52] on the JZ9-3 (Figure 6a) and the JZ20-2 platforms (Figure 6b). Previous studies suggested that the oceanic heat flux could be considered small or relatively constant, possibly filtered out [13]. For example, Cheng [13] considered the ocean heat flux as a constant of about  $2 \text{ Wm}^{-2}$  in the sea ice experiment conducted in 2002. In a recent study, Ma et al. [26] introduced a methodology for estimating the oceanic heat flux using the 2-m temperature measured at a meteorological station near the shores of Liaodong Bay. It is crucial to account for the daily fluctuations in the oceanic heat flux, with semi-diurnal tides exhibiting a dominant influence on the variability within Liaodong Bay. Moreover, the model results of sea ice thickness would be overestimated if the oceanic heat flux approaches  $0 \text{ Wm}^{-2}$ , such as in the study by Su et al. [52]. We examined the sea ice thickness under various parameterization schemes in the following section.

### 3.3. Nudging Sea Ice Thickness

The sea ice in Liaodong Bay during the season with sea ice cover is notoriously thin and challenging to forecast. Here, we employed the Nudging technique to incorporate initial values into the model. The fundamental concept of nudging involves incorporating a trend term into the model to minimize the disparity between the calculated and observed values. Specifically, retrieved sea ice thickness was included in the numerical model and linearly interpolated to align with each time step. Typically, the equation used for sea ice thickness forecasting is given as follows [55],

$$\frac{\partial h}{\partial t} = F(h, \vec{X}, t), \quad (5)$$

where  $h$  is the sea ice thickness,  $\vec{X}$  denotes a spatial independent variable,  $t$  denotes a temporal independent variable, and  $F$  is the forcing term. Here, we added a trend term to Equation (6),

$$\frac{\partial h}{\partial t} = F(h, \vec{X}, t) + G(h_{\text{obs}} - h_{\text{mod}}), \quad (6)$$

where  $G$  is the nudging factor, which represents the significance of the trend term. The nudging factor is typically determined based on the credibility of the observed data and the nudging coefficient. As an assimilation technique, nudging aims to minimize the difference between simulated values and observed values.  $h_{\text{obs}}$  is observed or retrieved sea ice thickness and  $h_{\text{mod}}$  is the simulated value of sea ice thickness. In this study, a data collection interval of every 5 days was implemented starting from the 25th day (25 December 2021). Wang et al. [56] applied trend terms in the assimilation technique of sea ice concentration while we directly assimilated the sea ice thickness. We determined  $G = 1/48$ , which showed the best fit. If nudging was applied, the sea ice thickness at the first timestep for nudging is determined by the simulated value from 25 h before the time when the initial values are added into the simulation. In the following 24 h, the observed or retrieved sea ice thickness would be nudged into the simulation during each time step. Following that, the HIGHTSI model would be employed to forecast the sea ice thickness for the next 5 days.

Figure 7 summarizes the simulation processes used for sea ice thickness in Liaodong Bay. We used a parameterized formula specifically designed for oceanic heat flux in this region. Subsequently, the model was subjected to meteorological forcing and oceanic heat flux inputs. The observed and retrieved sea ice thickness would be regarded as initial values if  $(\text{Day} - D_0)/N_i$  was a positive integer. Our nudging method effectively facilitated the generation of more moderate simulation. Additionally, a time series of the ice temperature and sea ice thickness at a specific location was generated.

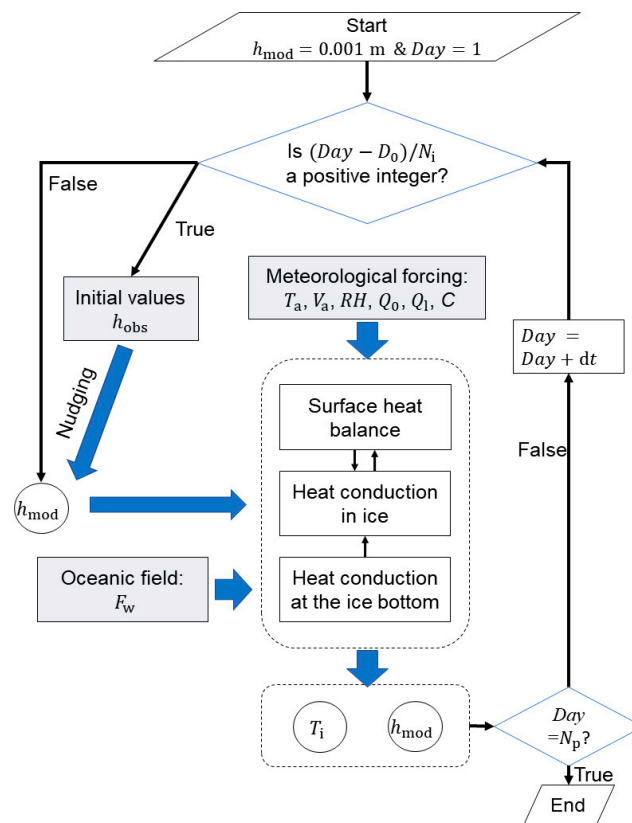


**Figure 7.** The simulation processes employed for the sea ice thickness in Liaodong Bay.

In Figure 7,  $Day$  denotes the number of days from 30 November,  $D_0$  is the date of initial ice formation,  $N_i$  denotes the time step of incorporating initial values,  $dt$  denotes the time step of the simulation,  $N_p$  denotes the total number of days in numerical simulations,  $T_a$  is 2-m temperature,  $V_a$  is 10-m wind velocity,  $RH$  is relative humidity,  $Q_0$  is downwards surface solar radiation,  $Q_1$  is downwards surface thermal radiation,  $C$  is total cloud cover,  $h_{mod}$  is the simulated sea ice thickness,  $h_{obs}$  is the retrieved sea ice thickness,  $T_i$  is ice temperature,  $F_w$  is oceanic heat flux. In this paper,  $D_0$  is equal to 25 for the date of initial ice formation and  $N_i$  is equal to 5. We assumed  $dt$  to be equal to 1/24 and  $N_p$  to be equal to 106 for the simulation period from 1 December 2021 to 15 March 2022.

In this section, we presented a parameterization scheme specifically tailored to the conditions within Liaodong Bay. Some parameters have uncertainties, including the construction of the heat exchange coefficient ( $c_h$ ). The mixed layer temperature stands out as a highly influential factor impacting the heat exchange coefficient ( $c_h$ ). Therefore, the accuracy of the reanalysis data pertaining to the mixed layer temperature assumes critical importance in the simulation outcomes. Moreover, the number of sea ice layers also affects the sea ice thickness simulation in Liaodong Bay. Considering the relatively low sea ice thickness in Liaodong Bay, it is appropriate to select a smaller number of sea ice layers in the numerical model.

#### 4. Results and Discussions

##### 4.1. Sea Ice Thickness Simulation, Forecasting, and Validation on the Two Oil Platforms

In this section, we reconstructed the sea ice thickness of the JZ20–2 and JZ9–3 platforms during the winter of 2021–2022. Firstly, different oceanic heat flux parameterization schemes were used for simulation in the HIGHTSI model. Subsequently, observed sea ice thickness was nudged into our simulations. The observations were introduced every 5 days starting from the 25th day (25 December 2021) on the JZ9–3 oil platform. On the JZ20–2 oil platform, assimilation occurred every 5 days from the 40th day (9 January 2022). It was important to note that not all daily observations were incorporated into the model. The number of

nudging techniques used in simulation on the JZ9–3 and the JZ20–2 oil platforms was 13 and 9, respectively. Finally, the accuracy of each scheme and the forecasting potential of nudging were evaluated by comparing the performance metrics.

Our simulation indicated that the JZ9–3 platform has a 65-day season with sea ice cover, as depicted in Figure 8a. Sea ice was presented from the 23rd day (23 December 2021) to the 87th day (25 February 2022) in the simulation. The JZ9–3 platform experienced two incidents of freezing, resulting in the sea ice thickness reaching its maximum on two separate occasions. Maximum sea ice thickness on the JZ9–3 oil platform occurred on the 43rd day (12 January 2022), approximately 12.5 cm. The general sea ice thickness on the JZ9–3 oil platform was 3–8 cm. Figure 8b presents the sea ice thickness for the JZ20–2 platform during the winter of 2021–2022. Our simulation indicated that the season with sea ice cover on the JZ20–2 oil platform lasted 52 days due to its lower latitude. The sea ice thickness on the JZ20–2 oil platform achieved its maximum three times. The maximum sea ice thickness of the JZ20–2 platform was observed on the 45th day (14 January 2022), approximately 8.9 cm, and the general sea ice thickness was approximately 2–7 cm.

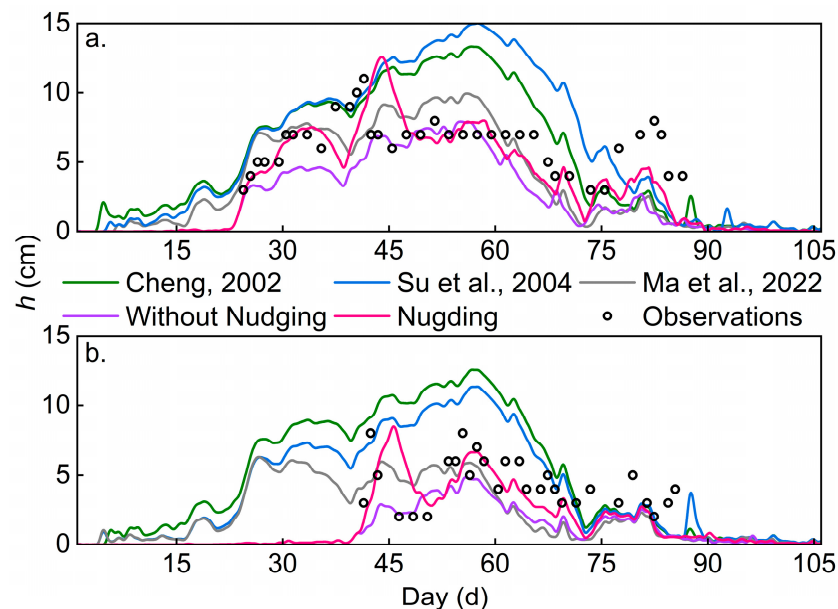


**Figure 8.** Sea ice thickness simulated by different parametrization schemes for oceanic heat flux on (a) the JZ9–3 and (b) the JZ20–2 oil platforms [13,26,52].

A comparison of sea ice thickness using different oceanic heat flux parametrization schemes is shown in Figure 8. All other parametrization schemes demonstrated that the simulation remained non-zero even during the ice-free period. The season with sea ice cover simulated in our scheme was more accurate than other parameterization schemes. Moreover, our parameterization scheme improved the accuracy of sea ice thickness during the initial ice period. The simulation, based on the schemes proposed by Cheng [13] and Su et al. [52], exhibited higher values compared to the observed data during severe ice period. In severe ice periods, it was inappropriate for the oceanic heat flux to be assumed as a particularly small value. That would carry an overestimation of sea ice thickness. Moreover, an abrupt increase in sea ice thickness on two oil platforms from the 40th to 45th day (9–14 January 2022) was successfully captured by the nudging technique.

The Root Mean Squared Error (RMSE) was used to evaluate the normalized distance between the observation and the simulation in different parameterization schemes [57], as shown in Table 2. Here, we divided the winter into three stages: stage 1 was before the severe ice period, stage 2 was the severe ice period, and stage 3 was after the severe ice period. Notably, both stage 1 and stage 3 included periods with and without sea ice cover during the winter of 2021–2022. On the JZ9–3 oil platform, the severe ice period lasted

from the 31st day (31 December 2022) to the 67th day (5 February 2022). The severe ice period lasted from the 52nd (20 January 2022) to the 70th day (8 February 2022) on the JZ20–2 oil platform. Compared to other schemes, our oceanic heat flux parameterization scheme decreased the RMSE by 0.53 cm and 2.90 cm on the JZ9–3 and the JZ20–2 oil platforms in stage 1, respectively. In stage 2, our oceanic heat flux parameterization scheme outperformed the parameterization schemes proposed by Cheng [13] and Su et al. [52]. Nudging resulted in a decrease of the RMSE to 1.73 cm and 1.60 cm on the JZ9–3 and the JZ20–2 oil platforms, respectively. In stage 3, the simulation performance of our oceanic heat flux parameterization scheme was similar to that of Ma et al. [26]. The application of the nudging method led to a reduction of approximately 1 cm in RMSE on the JZ9–3 oil platform during this period. However, the improvement on the JZ20–2 oil platform was not significant at that time.

**Table 2.** Root Mean Squared Error (RMSE) of simulated sea ice thickness using different parametrization schemes for oceanic heat flux on two oil platforms during the entire winter in 2021–2022.

Method	Platform	Stage		
		Stage 1	Stage 2	Stage 3
Nudging	JZ9–3	1.10 cm	1.73 cm	2.96 cm
	JZ20–2	1.25 cm	1.60 cm	1.21 cm
Without Nudging	JZ9–3	1.43 cm	2.20 cm	3.97 cm
	JZ20–2	1.43 cm	2.21 cm	1.21 cm
Cheng [13]	JZ9–3	2.13 cm	4.40 cm	3.66 cm
	JZ20–2	5.51 cm	4.75 cm	1.36 cm
Su et al. [52]	JZ9–3	1.91 cm	6.06 cm	3.81 cm
	JZ20–2	4.29 cm	3.77 cm	1.24 cm
Ma et al. [26]	JZ9–3	1.83 cm	2.12 cm	3.98 cm
	JZ20–2	3.19 cm	2.25 cm	1.22 cm

The forecasting potential was also evaluated using the RMSEs, as shown in Table 3. Here, we only compared the effectiveness of nudging and without nudging. The results indicated that the parameterization, which utilized the nudging method, demonstrated a good forecasting capability. The RMSE decreased in the simulations when nudging the observations on two oil platforms. Specifically, on the JZ9–3 and the JZ20–2 oil platforms, our simulations show a reduction in average RMSE of 0.78 cm, 0.77 cm, 0.75 cm, 0.68 cm, and 0.46 cm at 24, 48, 72, 96, and 120-h levels, respectively. It is worth noting that the RMSE might not show monotonic increases because the simulation was nudged every 5 days instead of adding an initial value daily for the next 5 days in this study. This method resulted in a limited number of samples. Nevertheless, our results demonstrated that nudging contributed to improved forecasting accuracy for sea ice thickness in general.

**Table 3.** Root Mean Squared Error (RMSE) of forecasting with and without nudging for predicting sea ice thickness on two oil platforms.

Method	Platform	Forecasting Hours				
		24 h	48 h	72 h	96 h	120 h
Nudging	JZ9–3	1.68 cm	2.02 cm	2.28 cm	2.38 cm	2.41 cm
	JZ20–2	1.64 cm	1.80 cm	1.92 cm	2.32 cm	1.80 cm
Without Nudging	JZ9–3	2.36 cm	2.80 cm	3.32 cm	3.34 cm	2.82 cm
	JZ20–2	2.51 cm	2.55 cm	2.37 cm	2.71 cm	2.31 cm

We observed that the RMSEs of simulations on the JZ9–3 oil platform were consistently higher than that on the JZ20–2 oil platform during the season with sea ice cover. The divergence observed between the two platforms highlights the uncertainty associated with

the meteorological and oceanographic data. Due to its proximity to the grid points, the JZ20–2 platform benefited from reanalyzed data that were more representative of the true value compared to the JZ9–3 platform. Additionally, the disparity could be attributed to the reliance on observation-based heat exchange coefficients from the JZ20–2 platform. The background conditions of other points were not taken into consideration when calculating the heat exchange coefficient. Consequently, our scheme resulted in a smaller RMSE for simulations conducted on the JZ20–2 oil platform compared to the JZ9–3 platform.

#### 4.2. Sea Ice Thickness Simulation in Liaodong Bay

Figure 9 presents a time series of sea ice thickness for the baseline depicted in Figure 1a. In the winter of 2021–2022, the baseline simulation had a season with sea ice cover from the 18th day (18 December 2021) to the 93rd day (3 March 2022). The majority of the simulated sea ice underwent melting after the 88th day (26 February 2022). Simulation with a thickness greater than 5 cm accounted for approximately 80 percent of the season with sea ice cover. The maximum simulated ice thickness of approximately 12.4 cm occurred on the 56th day (25 January 2022). However, this simulation did not represent the maximum ice thickness across the entire Liaodong Bay. Sea ice tended to accumulate on the east coast of Liaodong Bay during winter, primarily as a result of the prevailing north wind. Sea ice melting was observed in Liaodong Bay on the 72nd day (10 February 2022). At 2:00 a.m. on the 81st day (19 February 2022), the simulated ice edge was farthest from the northern beach, exceeding a distance of 100 km. However, sea ice thickness does not represent the maximum value at that time. Simulated sea ice thickness exhibited a decreasing trend along the baseline, from the inner part to the outer part of Liaodong Bay.

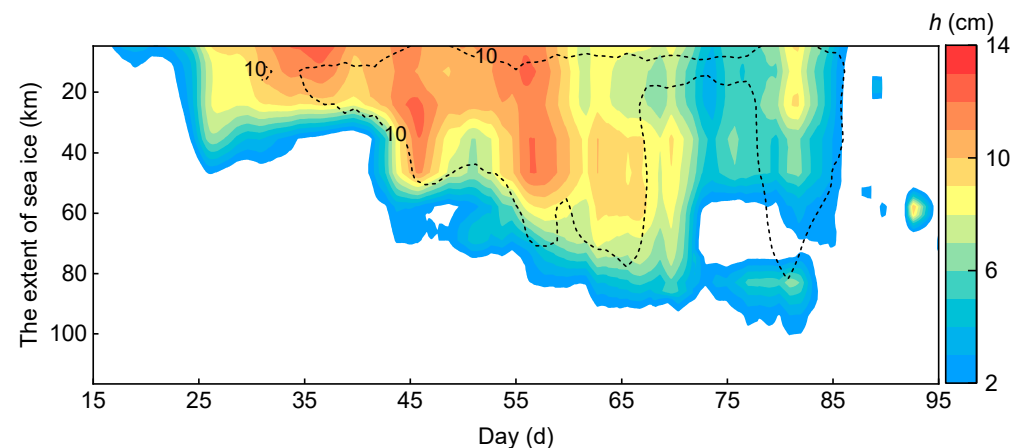


**Figure 9.** Time series of sea ice thickness on the baseline depicted in Figure 1a. Color contours are the forecasting ice thickness, and the black dotted line (10 cm) is the retrieved thickness.

The dashed line depicted in Figure 9 indicates the contour line of the retrieved sea ice with 10 cm thickness. Our findings indicated that the simulated sea ice thickness results align with the retrieved results observed during both the initial and severe ice periods. We speculated that the smaller simulated ice thickness was caused by a fluctuating decrease of 2-m air temperature during the second period of the large-scale freezing event.

Furthermore, we assessed the accuracy of nudging and compared results from different schemes in the selected region ( $40^{\circ}5' \sim 40^{\circ}50' \text{ N}$ ,  $121^{\circ}5' \sim 121^{\circ}50' \text{ E}$ ) (Figure 10). The findings indicated that lower oceanic heat fluxes could replicate the presence of sea ice with measurable thickness in unfrozen time during the initial ice period. Our parameterization scheme for oceanic heat fluxes had the potential to mitigate this issue because of incorporating temperature differences ( $\Delta T_m$ ). However, our oceanic heat flux parameterization scheme had a poor impact on sea ice simulation during the severe and melting ice periods. Nudging was more effective in improving the quality of the ice thickness simulation. For example, simulation without nudging underestimated the thickness by about 10–14 cm during the melting ice period, and the nudging process reduced this error

to less than 9 cm. In the selected area of Liaodong Bay, the R-squared values between the simulated and retrieved ice thickness demonstrated a strong correlation ( $R^2 = 0.92$ ) during the initial ice period. However, during the severe and melting ice periods, the correlation coefficients decreased to 0.67 and 0.55, respectively. For the entire season with sea ice cover, this R-squared value reached 0.76 in the selected area. Thus, our parametrization scheme for oceanic heat flux threw light on the areas with sea ice cover. Additionally, the implementation of nudging techniques resulted in a significant improvement in accuracy during the severe and melting ice periods.

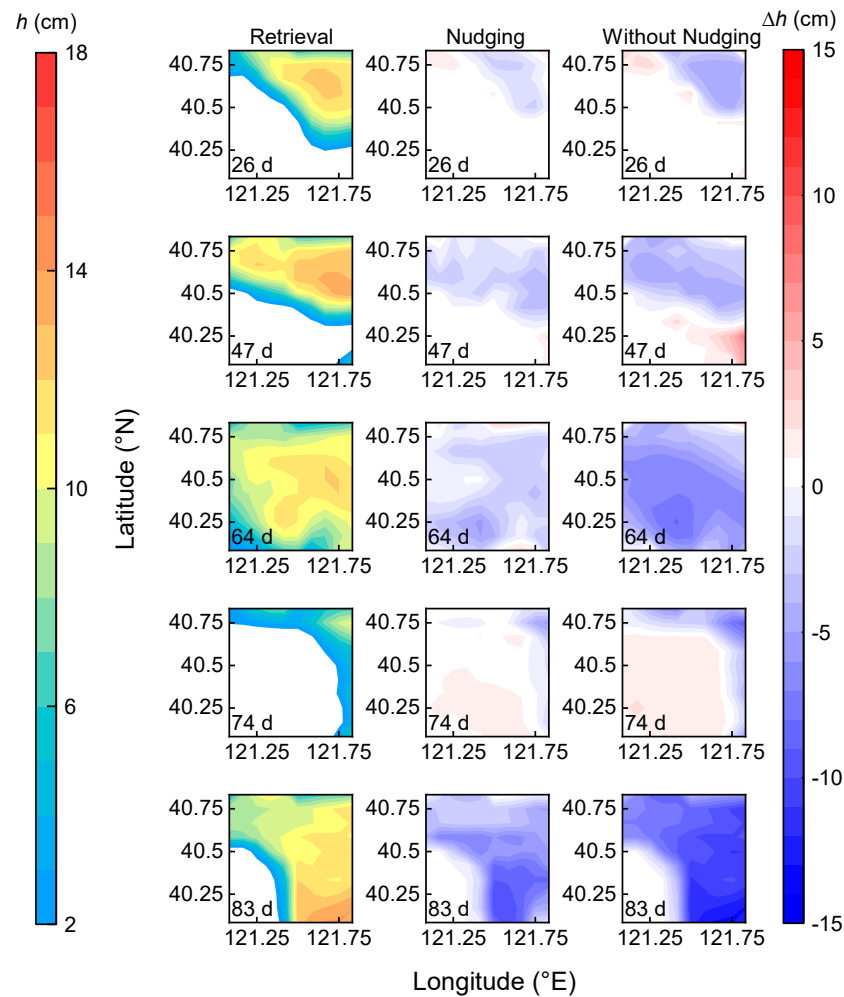


**Figure 10.** Simulated sea ice thickness with and without nudging, and the retrieved sea ice thickness within the region, 40°5′~40°50′ N, 121°5′~121°50′ E.

Figure 11 combines the satellite imagery and HIGHTSI simulated results. During the initial ice period, the sea ice distribution coincided well with the satellite imagery. The simulation did not show the low sea ice concentration observed near the outer edge. It was possibly due to low-resolution meteorological and oceanographic data during the severe ice period. Figure 11i shows a mismatch between the simulated and satellite sea ice distribution on the 87th day (15 February 2022). During the melting ice period, the thinner sea ice was more susceptible to the northwest winds towards the east coast of Liaodong Bay. Notably, larger values could occur nearshore (e.g., Figure 11d,h). Nearshore grid point air temperatures could approximate land temperatures. However, these errors would decrease with higher spatial and temporal resolution of meteorological and oceanic data.

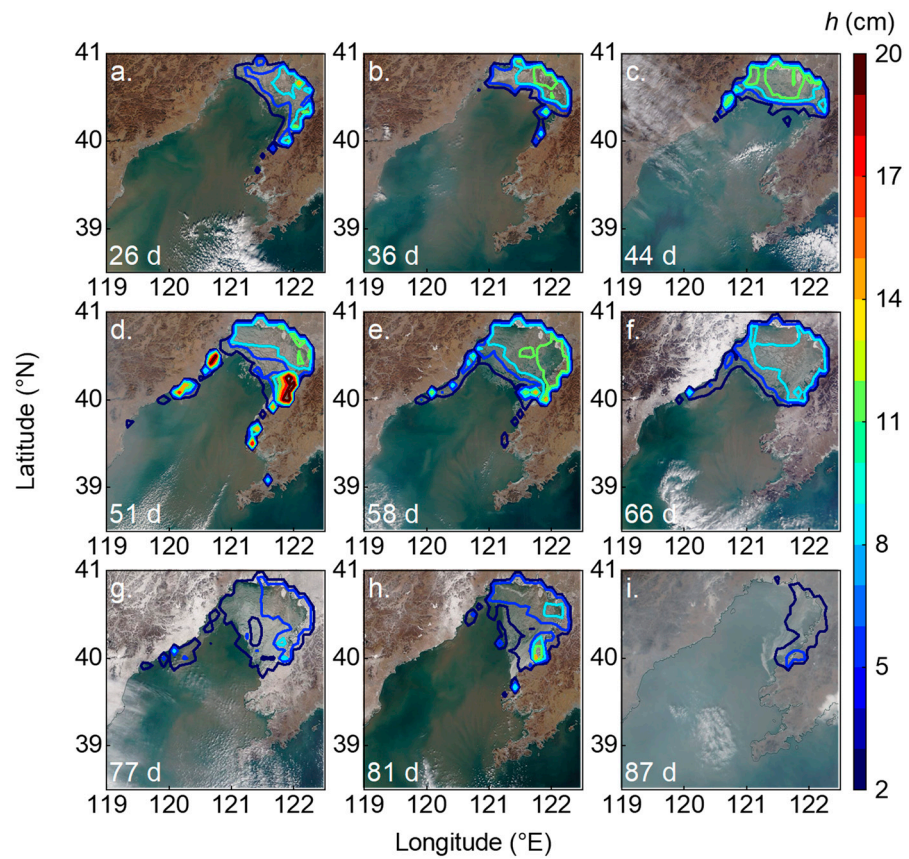


**Figure 11.** Comparison of the sea ice distribution between the simulation and the satellite images.

#### 4.3. Sea Ice Temperature

The ice temperature was recorded and presented in Figure 12. There were five ice layers in this study. Figure 12 shows the time series of air temperature and ice temperature for the JZ9–3 and JZ20–2 platforms. Both the JZ9–3 and JZ20–2 platforms encountered two seasons with sea ice cover throughout the entire winter. The first season with sea ice cover exhibited more significant variation compared to the second season with sea ice cover period. The ice temperature at different layers exhibited varying degrees of fluctuation in response to changes in temperature. Ice temperature sensitivity decreased as thickness increased. The layer in direct contact with seawater maintained the freezing point. On the JZ9–3 oil platform, the ice temperature reached its minimum on the 43rd day (12 January 2022), while the air temperature did not reach its lowest point. The minimum ice temperature was recorded on the 51st day (20 January 2022) following a cooling procedure on the JZ20–2 oil platform. Figure 12 indicates a period from the 72nd day (10 February 2022) to the 73rd day (11 February 2022) with no sea ice for the JZ9–3 and JZ20–2 platforms.

From Figure 12, we observed a noticeable delay in ice temperature compared to air temperature measurements. The average ice temperature was computed as the mean temperature of the first to fourth ice layers during freezing. The correlation coefficient of time lag was calculated to analyze the lag between the time series of ice temperature and air temperature [50]. Similarly, we established a correlation coefficient to quantify the impact of lag days in ice temperature response on daily average air temperature changes.

$$R_{dy}[T_a(t_d), T_i(t_{d+dy})] = \frac{\sum [T_a(t_d) - \overline{T_a(t_d)}][T_i(t_{d+dy}) - \overline{T_i(t_{d+dy})}]}{\sqrt{\sum [T_a(t_d) - \overline{T_a(t_d)}]^2 \sum [T_i(t_{d+dy}) - \overline{T_i(t_{d+dy})}]^2}}, \quad (7)$$

$$R_{dmax}[T_a(t_d), T_i(t_{d+dy})] = \max(R_{dy}[T_a(t_d), T_i(t_{d+dy})]), \quad (8)$$

where  $T_a$  is the air temperature,  $T_i$  is the average ice temperature from the first layer to the fourth layer.,  $t_d$  is current date,  $d_y$  denotes the number of days afterward,  $R_{d_y}$  denotes the daily correlation coefficient of time lag,  $R_{d_{max}}$  denotes the maximum daily correlation coefficient between the air temperature and the ice temperature.

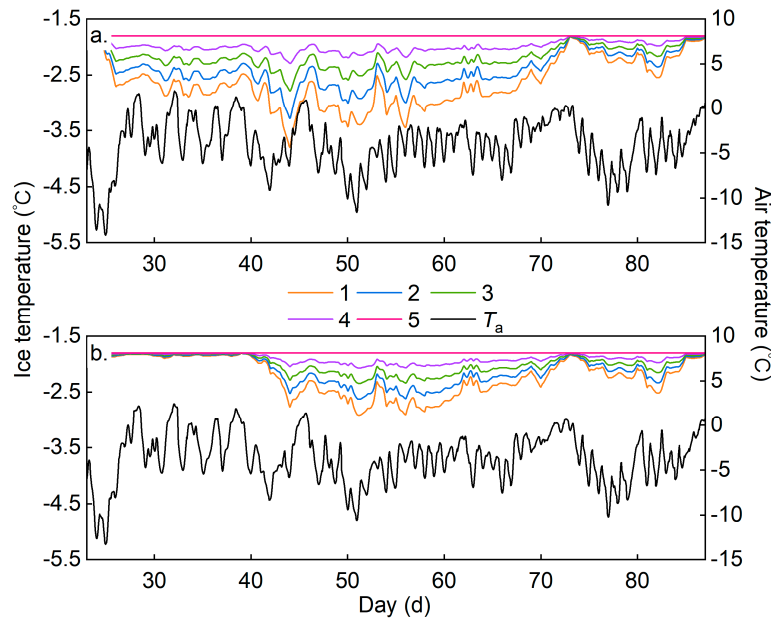


**Figure 12.** Ice temperature and air temperature of (a) the JZ9–3 and (b) the JZ20–2 oil platforms over the season with sea ice cover. (The colored lines represent ice temperature, with larger numbers in the legend indicating proximity to the ice bottom. The black line represents air temperature.).

For the JZ9–3 and JZ20–2 platforms, we computed the correlation coefficient pertaining to different time lags, ranging from 0 to 4 days. The corresponding outcomes were visually depicted in Figure 13a. Solid-marked points did not exhibit statistical significance at the 95% confidence level. Initially, the correlation coefficient of time lag exhibited an ascending trend followed by a subsequent decline after the next day. These findings indicated the existence of a time lag in the response between ice temperature and air temperature.

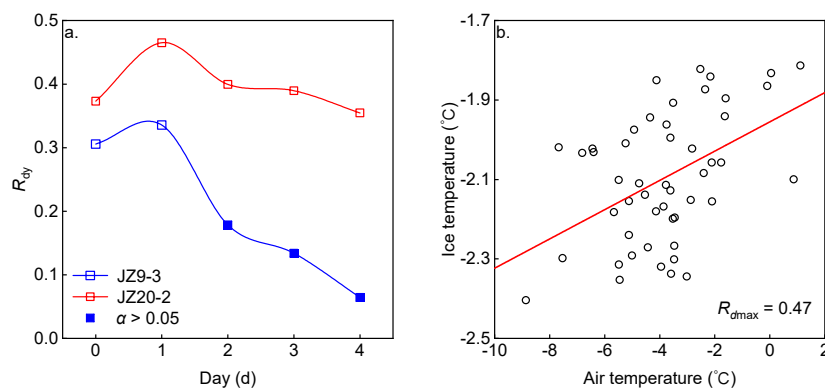


**Figure 13.** The relationship between the air temperature and the ice temperature. (a)  $R_{d_y}$  of the JZ9–3 and the JZ20–2 oil platforms and (b) the relationship between the daily average air temperature on the preceding day and the ice temperature during the season with sea ice cover at the JZ20–2 platform.

$R_{d_{max}}$  occurred on the second day after the temperature change, as shown in Figure 13a. It meant the daily average ice temperature had a one-day lag in response to air temperature. Surprisingly, the study did not find the highest correlation between ice temperature and air temperature on the same day. Figure 13b shows the air temperature and ice temperature corresponding to the point with the highest correlation coefficient ( $R_{d_{max}}$ ) in Figure 13a.

The daily average ice temperature displayed a positive and proportional correlation with the daily average air temperature on the preceding day, with the correlation coefficient of time lag.

The correlation coefficient confirmed the presence of similar variations in ice temperature and air temperature. Studies indicated that the air temperature was the primary factor that influenced the ice temperature. However, there is a clear hysteresis effect of ice temperature on air temperature. This effect is attributed to the hindrance of heat exchange between sea ice and the atmosphere due to the upper ice layer. Consequently, the response time of ice temperature to changes in air temperature is found to be delayed. At the same time, heat transfer between sea ice and the atmosphere is predominantly facilitated by the water vapor present at the interface between the sea ice and the air. This process leads to an increase in the thickness of the ice layer. The heat present in the sub-ice mixed layer is primarily derived from oceanic heat flux. However, the heat exchange between the mixed layer of seawater and the atmosphere becomes almost negligible. Thus, variations in air temperature have little impact on mixed-layer temperature.

In fact, the factors that influence ice temperature are complex. The ice temperature is subject to various meteorological factors, including air temperature, precipitation, snowfall, wind, and solar radiation. Hydrological factors such as water depth, surface area, and sea ice thickness also have an impact [58]. Moreover, the semi-enclosed nature of Liaodong Bay results in a higher concentration of contaminated ice. Hence, multiple factors contribute to a significant correlation coefficient of time lag between the ice temperature and air temperature in Liaodong Bay.

## 5. Conclusions

It is a challenge to simulate the growth and melting of sea ice with low thickness (<10 cm) because such sea ice undertakes a strong thermodynamic process. The sea ice model needs fine parameterization of oceanic heat flux with high temporal resolution. In this paper, we developed a new parameterization scheme for estimating the oceanic heat flux, which was applied in Liaodong Bay. This scheme was incorporated into the HIGHTSI model to simulate sea ice thickness during the winter of 2021–2022. The results demonstrated that our scheme significantly improved the accuracy in both ice-free and initial ice periods. The RMSE of sea ice thickness simulation by 0.53 cm and 2.90 cm on the JZ9–3 and the JZ20–2 oil platforms compared to other oceanic heat flux parameterization schemes. We applied the nudging method to the sea ice model to further bolster the forecasting accuracy. Abrupt changes in sea ice thickness were successfully captured by comparing the observed data from the JZ9–3 and JZ20–2 platforms. Our simulation showed that the root mean square errors on both observed points were less than 2 cm. Meanwhile, the Nudging method reduced the deviation by about 1–5 cm in the core region of Liaodong Bay. Our result agreed well with the sea ice distribution derived from the satellite images. Based on the proposed scheme, our findings indicated a moderate correlation ( $R = 0.47$ ) between the ice temperature and the air temperature of the previous day in Liaodong Bay. The proposed scheme offers a viable scheme to enhance the forecast accuracy and applies to various sea ice numerical models in Liaodong Bay.

**Author Contributions:** Conceptualization, B.W.; methodology, B.L., J.Z. and A.W.; software, B.W., Y.L. and A.W.; validation, Z.W.; formal analysis, B.W. and A.W.; investigation, B.W. and A.W.; data curation, J.Z.; writing—original draft preparation, B.W. and A.W.; writing—review and editing, B.W. and A.W.; visualization, B.W.; supervision, B.L. and A.W. All authors have read and agreed to the published version of the manuscript.

**Funding:** This research was supported by the National Natural Science Foundation of China (42176208) and the National Key Research and Development Program of China (2021YFC2801000).

**Data Availability Statement:** The data that support the findings of this study are available upon request from the first author upon reasonable request.

**Acknowledgments:** The authors thank Xi Liang and Fu Zhao for their valuable suggestions on the Nudge method and Dunwang Lu for proofreading this article.

**Conflicts of Interest:** The authors declare no conflict of interest.

## References

1. Yuan, S.; Gu, W.; Xu, Y.J.; Wang, P.; Huang, S.Q.; Le, Z.Y.; Cong, J.O. The estimate of sea ice resources quantity in the Bohai Sea based on NOAA/AVHRR data. *Acta Oceanol. Sin.* **2012**, *31*, 33–40. [[CrossRef](#)]
2. Ning, L.; Xie, F.; Gu, W.; Xu, Y.J.; Huang, S.Q.; Cui, W.J.; Yuan, S.; Levy, J. Using remote sensing to estimate sea ice thickness in the Bohai Sea, China based on ice type. *Int. J. Remote Sens.* **2009**, *30*, 4539–4552. [[CrossRef](#)]
3. Lang, W.H.; Wu, Q.; Zhang, X.; Meng, J.M.; Wang, M.; Cao, Y.J. Sea ice drift tracking in the Bohai Sea using geostationary ocean color imagery. *J. Appl. Remote Sens.* **2014**, *8*, 083650. [[CrossRef](#)]
4. Yan, Y.; Uotila, P.; Huang, K.Y.; Gu, W. Variability of sea ice area in the Bohai Sea from 1958 to 2015. *Sci. Total Environ.* **2020**, *709*, 136164. [[CrossRef](#)] [[PubMed](#)]
5. Ouyang, L.X.; Hui, F.M.; Zhu, L.X.; Cheng, X.; Cheng, B.; Shokr, M.; Zhao, J.C.; Ding, M.H.; Zeng, T. The spatiotemporal patterns of sea ice in the Bohai Sea during the winter seasons of 2000–2016. *Int. J. Digit. Earth* **2019**, *12*, 893–909. [[CrossRef](#)]
6. Gough, W.A.; Cornwell, A.R.; Tsuji, L.J.S. Trends in seasonal sea ice duration in southwestern Hudson Bay. *Arctic* **2004**, *57*, 299–305. [[CrossRef](#)]
7. Shugar, D.H.; Jacquemart, M.; Shean, D.; Bhushan, S.; Upadhyay, K.; Sattar, A.; Schwanghart, W.; McBride, S.; De Vries, M.V.W.; Mergili, M.; et al. A massive rock and ice avalanche caused the 2021 disaster at Chamoli, Indian Himalaya. *Science* **2021**, *373*, 300–306. [[CrossRef](#)] [[PubMed](#)]
8. Muhuri, A.; Bhattacharya, A.; Natsuaki, R.; Hirose, A. Glacier surface velocity estimation using Stokes vector correlation. In Proceedings of the 2015 IEEE 5th Asia-Pacific Conference on Synthetic Aperture Radar (APSAR), Singapore, 1–4 September 2015; pp. 606–609. [[CrossRef](#)]
9. Ma, Y.X.; Tan, H.J.; Yu, F.X.; Chen, X.; Yuan, S.; Xu, N.; Shi, W.Q. The evolution law and engineering application of ice thickness in Yingkou Sea area based on the thermodynamics of sea ice. *Marine Environ. Sci.* **2022**, *41*, 930–936. (In Chinese) [[CrossRef](#)]
10. Maykut, G.A.; Untersteiner, N. Some results from a time-dependent thermodynamic model of sea ice. *J. Geophys. Res.* **1971**, *76*, 1550–1575. [[CrossRef](#)]
11. Launiainen, J.; Cheng, B. Modelling of ice thermodynamics in natural water bodies. *Cold. Reg. Sci. Technol.* **1998**, *27*, 153–178. [[CrossRef](#)]
12. Cheng, B. On the numerical resolution in a thermodynamic sea-ice model. *J. Glaciol.* **2002**, *161*, 301–311. [[CrossRef](#)]
13. Cheng, B. On the Modelling of Sea Ice Thermodynamics and Air-Ice Coupling in the Bohai Sea and the Baltic Sea. Ph.D. Thesis, University of Helsinki, Helsinki, Finland, 2002. [[CrossRef](#)]
14. Cheng, B.; Vihma, T.; Pirazzini, R.; Granskog, M. Modelling of superimposed ice formation during the spring snowmelt period in the Baltic Sea. *Ann. Glaciol.* **2006**, *44*, 139–146. [[CrossRef](#)]
15. Cheng, B.; Mäkynen, M.; Simila, M.; Rontu, L.; Vihma, T. Modelling snow and ice thickness in the coastal Kara Sea, Russian Arctic. *Ann. Glaciol.* **2013**, *54*, 105–113. [[CrossRef](#)]
16. Cheng, B.; Vihma, T.; Rontu, L.; Kontu, A.; Pour, H.K.; Duguay, C.; Pulliainen, J. Evolution of snow and ice temperature, thickness and energy balance in Lake Orajärvi, northern Finland. *Tellus A* **2014**, *66*, 21564. [[CrossRef](#)]
17. Zhao, J.C.; Yang, T.; Shu, Q.; Shen, H.; Tian, Z.X.; Hao, G.H.; Zhao, B. Modelling the annual cycle of landfast ice near Zhongshan Station, East Antarctica. *Acta Oceanol. Sin.* **2021**, *40*, 129–141. [[CrossRef](#)]
18. Liu, C.W.; Hao, G.H.; Li, Y.B.; Zhao, J.C. The sensitivity of parameterization schemes in thermodynamic modeling of the landfast sea ice in Prydz Bay, East Antarctica. *J. Glaciol.* **2022**, *68*, 961–976. [[CrossRef](#)]
19. Bitz, C.M.; Lipscomb, W.H. An energy-conserving thermodynamic model of sea ice. *J. Geophys. Res.* **1999**, *104*, 15669–15677. [[CrossRef](#)]
20. Hibler, W.D.; Bryan, K. A diagnostic ice-ocean Model. *J. Geophys. Res. C. Oceans* **1987**, *17*, 987–1015. [[CrossRef](#)]
21. Lyrle, V.I.; Massom, R.; Bindoff, N.; Worby, A.; Allison, I. Wintertime heat flux to the underside of east Antarctic pack ice. *J. Geophys. Res. Biogeosci.* **2000**, *105*, 28759–28769. [[CrossRef](#)]
22. Ochiai, T.; Kakuta, S.; Iwasaki, S.; Nakata, K.; Sasaki, Y. Comparison of sensitivity of temperature and heat flux in sea-ice to change in air temperature between the Arctic Ocean and the Sea of Okhotsk. *J. Adv. Marine Sci. Technol. Soc.* **2009**, *15*, 173–179. [[CrossRef](#)]
23. Kirillov, S.; Dmitrenko, I.; Babb, D.; Rysgaard, S.; Barber, D. The effect of ocean heat flux on seasonal ice growth in Young Sound (Northeast Greenland). *J. Geophys. Res. Oceans* **2015**, *120*, 4803–4824. [[CrossRef](#)]
24. Ackley, S.F.; Xie, H.J.; Tichenor, E.A. Ocean heat flux under Antarctic sea ice in the Bellingshausen and Amundsen Seas: Two case studies. *Ann. Glaciol.* **2015**, *56*, 200–210. [[CrossRef](#)]
25. Lin, L.; Zhao, J.C. Estimation of oceanic heat flux under sea ice in the Arctic ocean. *J. Ocean Univ. China* **2019**, *18*, 605–614. [[CrossRef](#)]
26. Ma, Y.X.; Wang, Y.; Yu, F.; Xu, N.; Yuan, S.; Shi, W.Q. Research on the relationship between air temperatures, seawater temperature and ice regime in winter during 2017–2018 at the adjacent sea of Hongyanhe, Liaodong Bay. *J. Glaciol. Geocryol.* **2022**, *44*, 1482–1491. (In Chinese) [[CrossRef](#)]

27. Ji, S.Y.; Yue, Q.J. Determination and analysis of oceanic Heat Flux under sea ice cover in the Liaodong Bay. *Mar. Sci. Bull.* **2000**, *2*, 41–48. (In Chinese)
28. Su, J.; Wu, H.D.; Zhang, Y.F.; Bai, S.; Liu, Q.Z. A coupled ice-ocean model for the Bohai Sea: II. Case study. *Acta. Oceanol. Sin.* **2005**, *24*, 54–67. [[CrossRef](#)]
29. Wang, K.; Liu, P.; Jin, S.; Wang, N.; Yu, Z. Sea-ice growth and decay model of Bohai Sea based on thermodynamic process. *Adv. Water. Sci.* **2017**, *28*, 116–123. (In Chinese) [[CrossRef](#)]
30. Deser, C.; Tomas, R.A.; Sun, L. The role of ocean-atmosphere coupling in the zonal-mean Atmospheric response to Arctic sea ice loss. *J. Climate* **2015**, *28*, 2168–2186. [[CrossRef](#)]
31. Deser, C.; Tomas, R.A.; Screen, J. Does ocean coupling matter for the northern extratropical response to projected Arctic sea ice loss? *Geophys. Res. Lett.* **2016**, *43*, 2149–2157. [[CrossRef](#)]
32. Sun, L.; Alexander, M.; Deser, C. Evolution of the global coupled climate response to Arctic sea ice loss during 1990–2090 and its contribution to climate change. *J. Climate* **2018**, *31*, 7823–7843. [[CrossRef](#)]
33. Dai, A.G.; Luo, D.H.; Song, M.R.; Liu, J.P. Arctic amplification is caused by sea-ice loss under increasing CO<sub>2</sub>. *Nat. Commun.* **2019**, *10*, 121. [[CrossRef](#)]
34. Suo, L.L.; Gao, Y.Q.; Guo, D.; Bethke, I. Sea-ice free Arctic contributes to the projected warming minimum in the North Atlantic. *Environ. Res. Lett.* **2017**, *12*, 074004. [[CrossRef](#)]
35. Smith, D.M.; Dunstone, N.J.; Scaife, A.A.; Fiedler, E.K.; Copsey, D.; Hardiman, S.C. Atmospheric response to Arctic and Antarctic sea ice: The importance of ocean-atmosphere coupling and the background state. *J. Climate* **2017**, *30*, 4547–4565. [[CrossRef](#)]
36. Audette, A.; Kushner, P.J. Simple hybrid sea ice nudging method for improving control over partitioning of sea ice concentration and thickness. *J. Adv. Model. Earth Syst.* **2022**, *14*, e2022MS003180. [[CrossRef](#)]
37. GB/T 42254-2022; Sea Ice Grade of Bohai Sea and Northern Yellow Sea. National Technical Committee 283 on Ocean of Standardization Administration of China: Beijing, China, 2022.
38. ERA5 Hourly Data on Single Levels from 1940 to Present. Available online: <https://cds.climate.copernicus.eu/cdsapp#!/dataset/reanalysis-era5-single-levels?tab=overview> (accessed on 4 October 2023).
39. Global Ocean Physics Analysis and Forecast. Available online: [https://data.marine.copernicus.eu/product/GLOBAL\\_ANALYSISFORECAST\\_PHY\\_001\\_024/download?dataset=cmems\\_mod\\_glo\\_phy\\_anfc\\_0.083deg\\_PT1H-m](https://data.marine.copernicus.eu/product/GLOBAL_ANALYSISFORECAST_PHY_001_024/download?dataset=cmems_mod_glo_phy_anfc_0.083deg_PT1H-m) (accessed on 4 October 2023).
40. Wang, Z.Y.; Liu, G.M.; Wang, H.; Wang, D.K. Numerical study of seasonal and interannual variation of circulation and water transports in the Luzon Strait. *Acta. Oceanol. Sin.* **2016**, *38*, 1–13. (In Chinese) [[CrossRef](#)]
41. Key, J.R.; Silcox, R.A.; Stone, R.S. Evaluation of surface radiative flux parameterizations for use in sea ice models. *J. Geophys. Res. Atmos.* **1996**, *101*, 3839–3850. [[CrossRef](#)]
42. Shine, K.P. Parametrization of the shortwave flux over high albedo surfaces as a function of cloud thickness and surface albedo. *Q. J. R. Meteorol. Soc.* **1984**, *110*, 747–764. [[CrossRef](#)]
43. Prata, A.J. A new long-wave formula for estimating downward clear-sky radiation at the surface. *Q. J. R. Meteorol. Soc.* **1996**, *122*, 1127–1151. [[CrossRef](#)]
44. Bennett, T.J. A coupled atmosphere-sea ice model study of the role of sea ice in climatic predictability. *J. Atmos. Sci.* **1982**, *39*, 1456–1465. [[CrossRef](#)]
45. Jacobs, J.D. Radiation climate of Broughton Island. In *Energy Budget Studies in Relation to Fast-Ice Breakup Processes in Davis Strait*; Institute of Arctic and Alpine Research: Boulder, CO, USA, 1978; pp. 105–120.
46. Grenfell, T.; Maykut, G. The optical properties of ice and snow in the Arctic Basin. *J. Glaciol.* **1977**, *18*, 445–463. [[CrossRef](#)]
47. Perovich, D.K. Complex yet translucent: The optical properties of sea ice. *Physica B Condens. Matter* **2003**, *338*, 107–114. [[CrossRef](#)]
48. Untersteiner, N. On the mass and heat budget of arctic sea ice. *Arch. Met. Geoph. Biokl.* **1961**, *12*, 151–182. [[CrossRef](#)]
49. Josberger, E.G. Bottom ablation and heat transfer coefficients from the 1983 Marginal Ice Zone Experiments. *J. Geophys. Res. Atmos.* **1987**, *92*, 7012–7016. [[CrossRef](#)]
50. Lei, R.B.; Li, Z.J.; Zhang, Z.H.; Cheng, Y.F. Thermodynamic processes of lake ice and landfast ice around Zhongshan Station, Antarctica. *China J. Polar Res.* **2011**, *22*, 143–152. (In Chinese) [[CrossRef](#)]
51. Chen, X.D.; Høyland, K.; Wang, A.L.; Ji, S.Y. Determination of heat transfer coefficient on water-ice interface under free convection condition. *Acta. Oceanol. Sin.* **2018**, *40*, 140–148. (In Chinese)
52. Su, J.; Wu, H.D.; Zhang, Y.F.; Liu, Q.Z.; Shan, B. A coupled ice-ocean model for the Bohai Sea I. Study on model and parameter. *Acta. Oceanol. Sin.* **2004**, *23*, 597–608. (In Chinese) [[CrossRef](#)]
53. Jacob, S.; Panteleev, G.; Kirillov, S.A.; Makhotin, M.; Shakhova, N. Sea-surface temperature and salinity product comparison against external in situ data in the Arctic Ocean. *J. Geophys. Res. Oceans* **2015**, *120*, 7223–7236. [[CrossRef](#)]
54. Ji, S.Y.; Yue, Q.J.; Bi, X.J. Heat transfer coefficient between ice cover and water in the Bohai Sea. *Marine Sci. Bull.* **2002**, *21*, 9–15. (In Chinese) [[CrossRef](#)]
55. Li, C.H.; Liu, Y.; Bai, S.; Zhang, Q.W.; Li, B.H. Numerical sea ice forecast for the Bohai Sea in the winter of 2004–2005. *Marine Forecast.* **2006**, *23*, 1–8. (In Chinese) [[CrossRef](#)]
56. Wang, K.G.; Debernard, J.; Sperreik, A.K.; Isachsen, P.E.; Lavergne, T. A combined optimal interpolation and nudging scheme to assimilate OSISAF sea-ice concentration into ROMS. *Ann. Glaciol.* **2013**, *54*, 8–12. [[CrossRef](#)]

57. Muhuri, A.; Gascoin, S.; Menzel, L.; Kostadinov, T.S.; Harpold, A.A.; Valledado, A.S.; Lopez-Moreno, J.I. Performance Assessment of Optical Satellite-Based Operational Snow Cover Monitoring Algorithms in Forested Landscapes. *IEEE J. Sel. Top. Appl. Earth Obs. Remote Sens.* **2021**, *14*, 7159–7178. [[CrossRef](#)]
58. Brown, L.C.; Duguay, C.R. The response and role of ice cover in lake-climate interactions. *Prog. Phys. Geogr. Earth Environ.* **2010**, *34*, 671–704. [[CrossRef](#)]

**Disclaimer/Publisher’s Note:** The statements, opinions and data contained in all publications are solely those of the individual author(s) and contributor(s) and not of MDPI and/or the editor(s). MDPI and/or the editor(s) disclaim responsibility for any injury to people or property resulting from any ideas, methods, instructions or products referred to in the content.